Intermolecular conical intersections in molecular aggregates

Antonietta De Sio [1,9] ✉, Ephraim Sommer[1,9], Xuan Trung Nguyen[1], Lynn Groß[2], Duško Popović[3], Benjamin Tyler Nebgen[4], Sebastian Fernandez-Alberti [5], Stefano Pittalis[6], Carlo Andrea Rozzi [6], Elisa Molinari[6,7], Elena Mena-Osteritz[3], Peter Bäuerle[3], Thomas Frauenheim[2,8], Sergei Tretiak [4] and Christoph Lienau [1]

Conical intersections (CoIns) of multidimensional potential energy surfaces are ubiquitous in nature and control pathways and yields of many photo-initiated intramolecular processes. Such topologies can be potentially involved in the energy transport in aggregated molecules or polymers but are yet to be uncovered. Here, using ultrafast two-dimensional electronic spectroscopy (2DES), we reveal the existence of intermolecular CoIns in molecular aggregates relevant for photovoltaics. Ultrafast, sub-10-fs 2DES tracks the coherent motion of a vibrational wave packet on an optically bright state and its abrupt transition into a dark state via a CoIn after only 40 fs. Non-adiabatic dynamics simulations identify an intermolecular CoIn as the source of these unusual dynamics. Our results indicate that intermolecular CoIns may effectively steer energy pathways in functional nanostructures for optoelectronics.

In a basic example of intramolecular conical intersections (CoIns)[1–3], crossings between multidimensional potential energy surfaces (PESs) of an optically bright (S_2) and a dark (S_1) excited electronic state arise from the coupling of these states to at least two vibrational modes of the molecule (Fig. 1). In the simplest topology, coupling to a symmetric mode (Q_1) displaces the CoIn (star) from the Franck–Condon region (dot) of the molecule[4]. The two electronic states are vibronically coupled via an asymmetric vibrational mode (Q_2), resulting in an essentially conical shape of the PES near the CoIn and a complete breakdown of the Born–Oppenheimer approximation in this region[1,3]. From a dynamical perspective, the impulsive optical excitation of such a molecule launches a vibrational wave packet in the Franck–Condon region of the bright state S_2 and triggers its coherent motion towards the CoIn. Here, vibronic couplings induce an ultrafast non-adiabatic transition into the dark state S_1. This transition is essentially barrierless and reflection-free[5] and may be accompanied by substantial wave packet spreading on surface crossing[1,2]. Hence, intramolecular CoIns provide channels for efficient, directional energy and charge flow within molecules that are actively governed by molecular vibrations. CoIns control the dynamics and yield of elementary reactions underlying many chemical and biological functions[6–8]. Important examples are the photoisomerization of retinal, initiating the primary event of vision[6,9–12], the photochemistry of synthetic molecular switches[13–17], intramolecular vibrational relaxation in carotenoids[18], DNA protection against photodamage[19,20], singlet exciton fission[21] and potentially even the primary steps in the magnetoreception of birds[22,23].

In principle, CoIns may also be relevant for controlling energy or charge transport in extended condensed-phase assemblies, such as polymer or molecular aggregates. In such systems, vibronic couplings promote delocalization of the excitations across many molecular units and control their coherent transport on the nanoscale[24,25]. Intermolecular CoIns may thus affect this transport. While recent theoretical work started to investigate the potential role of intermolecular CoIns for exciton transfer dynamics[26–28], experimental observations have not been presented so far.

Here we report distinct signatures of the passage of a wave packet through an intermolecular CoIn in the two-dimensional (2D) electronic spectroscopy (2DES) maps of an oligomer thin film relevant for organic photovoltaics. We find that the optically launched vibrational wave packet crosses the CoIn after just around 40 fs and that this passage is accompanied by an abrupt change in the 2DES maps. Atomistic non-adiabatic dynamics simulations confirm the intermolecular nature of the CoIn.

Ultrafast 2D electronic spectroscopy of thin films

We investigate thin films of a solution processable acceptor–donor–acceptor-type (A–D–A) oligomer[29] consisting of two terminal dicyanovinyl groups as acceptor and a central dithienopyrrole-thiophene unit as donor (Fig. 1c, upper panel). These oligomers represent an important class of organic building blocks that have recently emerged as efficient photoactive materials in different optoelectronic applications such as organic photovoltaics, light-emission, sensors and transistors[30–32]. Our A–D–A oligomer finds application as the main light absorber and p-type molecular semiconductor in efficient solution-processed organic solar cells reaching power conversion efficiencies of >8% (refs. [29,33]). In the thin films, the A–D–A oligomers build highly ordered nanoscale aggregates

[1]Institut für Physik and Center of Interface Science, Carl von Ossietzky Universität, Oldenburg, Germany. [2]Bremen Center for Computational Materials Science, University of Bremen, Bremen, Germany. [3]Institut für Organische Chemie II and Neue Materialien, Universität Ulm, Ulm, Germany. [4]Theoretical Division, Los Alamos National Laboratory, Los Alamos, NM, USA. [5]National University of Quilmes/CONICET, Department of Science and Technology, Bernal (B1876BXD), Buenos Aires Province, Argentina. [6]Istituto Nanoscienze—CNR, Modena, Italy. [7]Università di Modena e Reggio Emilia, Dipartimento di Scienze Fisiche, Informatiche e Matematiche, Modena, Italy. [8]Computational Science Research Center, Beijing and Computational Science and Applied Research Institute Shenzhen, Shenzhen, China. [9]These authors contributed equally: Antonietta De Sio, Ephraim Sommer. ✉e-mail: antonietta.de.sio@uni-oldenburg.de
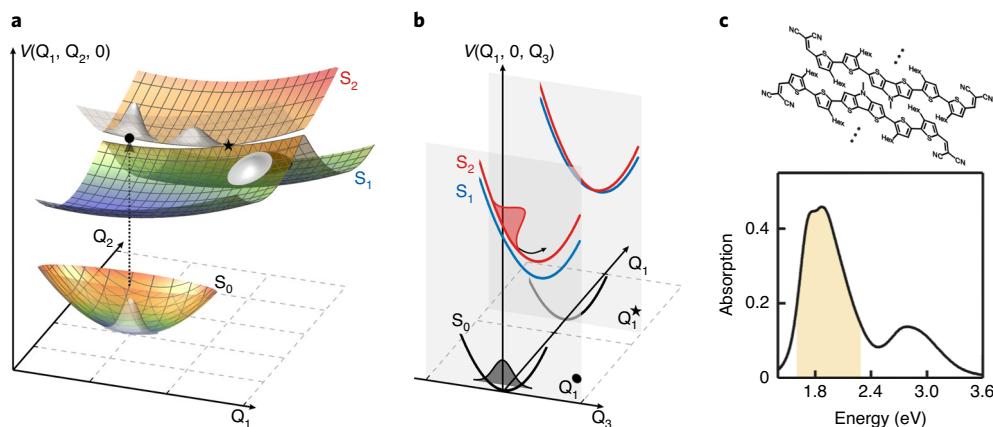
Fig. 1 | Schematic illustration of wave packet motion through a conical intersection (CoIn) in the potential energy surface $V(Q_1, Q_2, Q_3)$ of an A–D–A oligomer aggregate. a,b, Driven by vibronic coupling to the tuning modes (Q_1, Q_3), a vibrational wave packet on the bright S_2 excited state of the aggregate potential, optically launched in the Franck–Condon region (dot), moves towards the CoIn (star), oscillating along Q_3 (**b**). Near the CoIn, strong vibronic coupling to the coupling mode (Q_2) induces an ultrafast and efficient non-adiabatic transition from S_2 to the optically dark excited state S_1. **c,** Chemical structure of the oligomer aggregate (upper panel) showing an antiparallel arrangement, together with the measured linear absorption spectrum (lower panel) of the thin film. The yellow shaded area indicates the excitation energy range used in the experiments.

with grain sizes of roughly 20–50 nm (ref. [33]). The linear absorption spectrum of the thin film (Fig. 1c, lower panel) shows two broad absorption bands around 1.9 eV (shaded yellow) and 2.8 eV reflecting optically bright exciton transitions of the aggregate. On the broad, low-energy resonance at 1.9 eV, we note a very slight peak structure reflecting a vibrational progression of the S_0–S_2 transition (Supplementary Fig. 6).

For the 2DES[34] experiments, the thin films are excited by broadband 8-fs pulses resonant with the low-energy resonance at 1.9 eV. The spectra are recorded at room temperature in a partially collinear geometry, using a pair of phase-locked excitation pulses, time-delayed by the coherence time τ and the probe beam, arriving at waiting time T (Fig. 2a and Supplementary Fig. 1). At selected T, differential transmission spectra are obtained as a function of τ and of the detection energy E_D. This time-domain signal $S(\tau, T, E_D)$ is then evaluated according to the procedure outlined in the Methods section to obtain the 2DES energy–energy maps (Fig. 2). Briefly, at each T, we perform a Fourier transform of $S(\tau, T, E_D)$ along τ, which yields complex valued 2D maps as a function of the excitation energy E_X and E_D. By taking the real part of these Fourier transform maps at each T, we obtain the absorptive 2DES energy–energy maps[34] $A_{2D}(E_X, T, E_D)$ as a function of E_X and E_D. All experimental details are reported in the Methods section.

At early waiting times, $T < 20$ fs, the 2DES spectra of the aggregate thin film show a well-defined, grid-like peak pattern with two dominant diagonal peaks at 1.87 eV and roughly 2.0 eV and a series of cross peaks (Fig. 2b–d). Such grid-like patterns generally reflect the impulsive optical excitation of coherent vibrational wave packets with one dominant oscillation period on either the ground or excited-state PES[36,37]. As we will argue below, the peak spacings of roughly 132 meV along E_D indicate an oscillation with a period of around 30 fs as the dominant Franck–Condon-active mode[36,38,39] on the bright excited S_2 state of the aggregate (Fig. 2b, dashed white lines). For larger waiting times, 20 fs $< T < 45$ fs, significant spectral modifications of the 2DES pattern occur. In particular, we observe a rapid reduction of the peak spacing along E_D (Fig. 2e–g and Supplementary Fig. 4). After $T \cong 45$ fs, the 2DES maps are fundamentally different, as a much broader diagonal peak around 1.94 eV is seen (Fig. 2h and Supplementary Fig. 4). While the peak spacings along E_D have almost completely washed out, a weak structure remains along E_X (Fig. 2i,j). No further spectral modifications can

be observed for longer T (Supplementary Fig. 4). The white dashed lines in Fig. 2b–j indicate the grid pattern seen at early times and underline the substantial spectral changes. At all investigated waiting times, we observe positive peaks A_{2D} suggesting that the dominant contributions to the 2DES signal arise from bleaching and stimulated emission transitions.

The pump–pulse pair in our experiment (1–2 in Fig. 2a) mainly induces optical transitions between the ground and bright S_2 excited state in the Franck–Condon region. For systems that are reasonably well described by displaced harmonic oscillator PESs, this results in 2DES maps with equidistantly spaced peaks along both the excitation E_X and detection E_D axes[36,39,40]. These peak spacings are determined by the frequency of the coupled vibrational mode(s). Such a grid-like peak pattern is indeed seen in our 2DES experiment (Fig. 2b–d). Fourier transform along E_X and E_D thus provides the dominant period(s) of the Franck–Condon-active vibrations. Coupling of these vibrations to the electronic states displaces the electronic excited-state PES with respect to the ground state equilibrium geometry and these vibrations hence represent tuning modes. Our 2DES data thus indicate a fast tuning mode (Q_3) frequency of roughly 1,100 cm^{-1} (about 30 fs).

In our experiment, we observe reductions of the peak spacing along E_D for 20 fs $< T < 45$ fs (Fig. 2e–g). Such surprising changes cannot be easily rationalized purely on the basis of harmonic oscillator PESs. Raman spectra of our thin film (Supplementary Fig. 15) show a series of well-resolved peaks, as is typical for a multimode, basically harmonic ground state PES. Wave packet motion on such a PES cannot account for the time-dependent peak shifts[36,40]. We therefore deduce that this variation of the peak spacing results mainly from the motion of the optically launched excited-state wave packet in our sample. Specifically, a transient change in the peak spacing, and thus in the instantaneous vibrational frequency, may arise from the motion of the excited-state wave packet into a PES region with different local curvature. Fourier transform of our 2DES data along E_D thus reveals a marked, rapid increase of the instantaneous oscillation period (Fig. 2k shaded), pointing to a significant anharmonicity of the excited S_2 PES experienced by the excited-state wave packet. During this waiting time window, we also observe a substantial drop of the 2DES peak amplitude A_{2D} (Supplementary Fig. 5), which reaches a quasi-stationary value after $T \cong 45$ fs. Concurrently, also the Fourier transform intensity at the
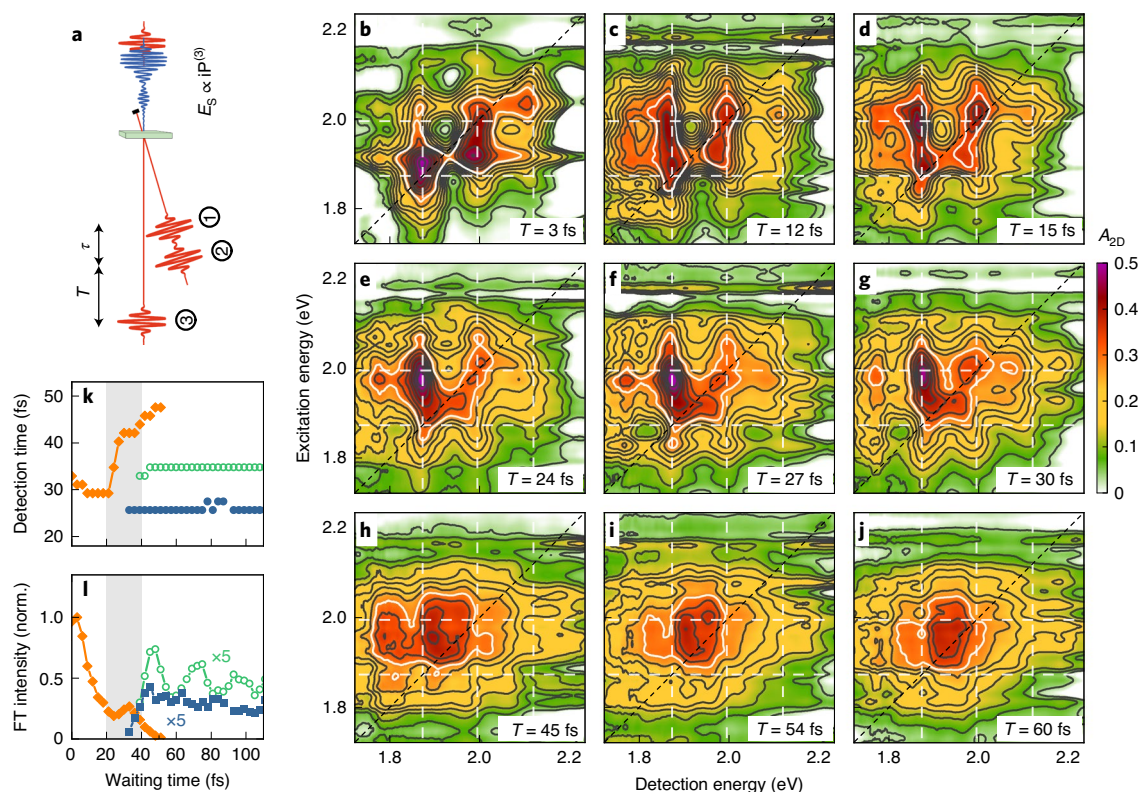
Fig. 2 | 2DES probes wave packet motion through an intermolecular conical intersection (CoIn) in a thin film of molecular aggregates. a, Scheme of the pulse-sequence interacting with the sample, indicating the coherence τ and waiting T times. The field E_s (blue) re-emitted by the sample is proportional to the nonlinear polarization $P^{(3)}$ induced in the sample by the interaction with the pulse sequence. **b–d**, For $T < 20$ fs, the 2DES maps show a grid-like peak pattern revealing coherent vibrational wave packet motion on the S_2 state with a roughly 30-fs period (white dashed lines). **e–g**, For 20 fs $< T < 40$ fs, the peak spacing along the detection axis gradually reduces, pointing to anharmonicities of the S_2 state potential. **h–j**, At $T \cong 45$ fs, the grid pattern disappears and the 2DES spectra become essentially featureless. This transition marks the passage through the CoIn. **k–l**, Waiting time dynamics of the period (**k**) and amplitude (**l**) of the dominant vibrational modes, extracted from a Fourier transform (FT) analysis of the 2DES maps along the detection axis. Initially, $T < 20$ fs, only one 30-fs mode (**k**, orange) dominates, before its oscillation period gradually increases. At $T \cong 45$ fs, the amplitude of this mode drops completely (**l**, orange) and new, distinctly different oscillatory modes with ~24 fs (**k**, blue) and 35 fs (**k**, green) periods appear. norm., normalized.

period of the Q_3 mode drops and vanishes (Fig. 2l, orange). Both these observations suggest an ultrafast depopulation of the excited S_2 bright state.

For $T > 45$ fs, distinctly new oscillatory components, with periods of roughly 24 and 35 fs, and much weaker Fourier transform intensity, are seen (Fig. 2k–l, blue and green). They persist essentially unchanged for longer waiting times, at least up to around 200 fs. Since the ground state bleaching contribution to the 2DES map remains even after depopulation of the S_2 state, the new oscillatory features most probably reflect coherent ground state vibrational motion.

Together, all these experimental signatures strongly indicate that we follow a surface crossing from an optically bright S_2 to a dark excited state S_1 that proceeds through a CoIn. The time evolution of the grid pattern in the 2DES maps suggests that it takes roughly 45 fs for the optically launched S_2 wave packet to reach and pass the CoIn. Hence, taking this timescale as one half of the vibrational period of the tuning mode Q_1, we deduce a vibrational frequency of at least $\nu(Q_1) \lesssim 2\pi/90 \, \text{fs}^{-1}$ for the reaction coordinate. The pronounced anharmonicity in S_2 wave packet motion and the abrupt changes in vibrational frequencies at $T \cong 45$ fs provide additional evidence for the existence of a CoIn in the multidimensional PES of the aggregates.

We have compared these dynamics with those of a dichloromethane solution of the A–D–A oligomer, where aggregation is

completely suppressed. In pump-probe spectra, we observe broad and featureless resonances showing no significant changes on a sub-100-fs timescale (Supplementary Fig. 3). Since these measurements probe the intramolecular dynamics of the A–D–A backbone, we find that the peculiar, sub-50-fs dynamics are a distinct feature of the solid-state nanostructure of the aggregated thin film and they are of an intermolecular nature.

All these experimental results strongly indicate non-adiabatic dynamics induced by vibronic couplings in the vicinity of an intermolecular CoIn in the potential energy landscape of the aggregate oligomer thin film.

Non-adiabatic dynamics simulations
To validate these arguments, we investigate the photoinduced pathways by non-adiabatic excited-state molecular dynamics simulations[41,42]. In a single A–D–A oligomer, the low-energy intramolecular optical excitations mainly have contributions from the lowest excited state S_1^M of the monomeric, oligomer backbone, which is optically bright (Supplementary Fig. 7). All other excited states lie higher in energy and we find no evidence for the existence of intramolecular CoIns in the energy range of interest. We therefore consider dimers of the A–D–A oligomer as a minimal model system for the aggregates forming in our thin films (Fig. 1c, upper panel). In contrast to a single oligomer, here, we find that the lowest-lying excited state S_1 is optically dark (Supplementary Fig. 8b).
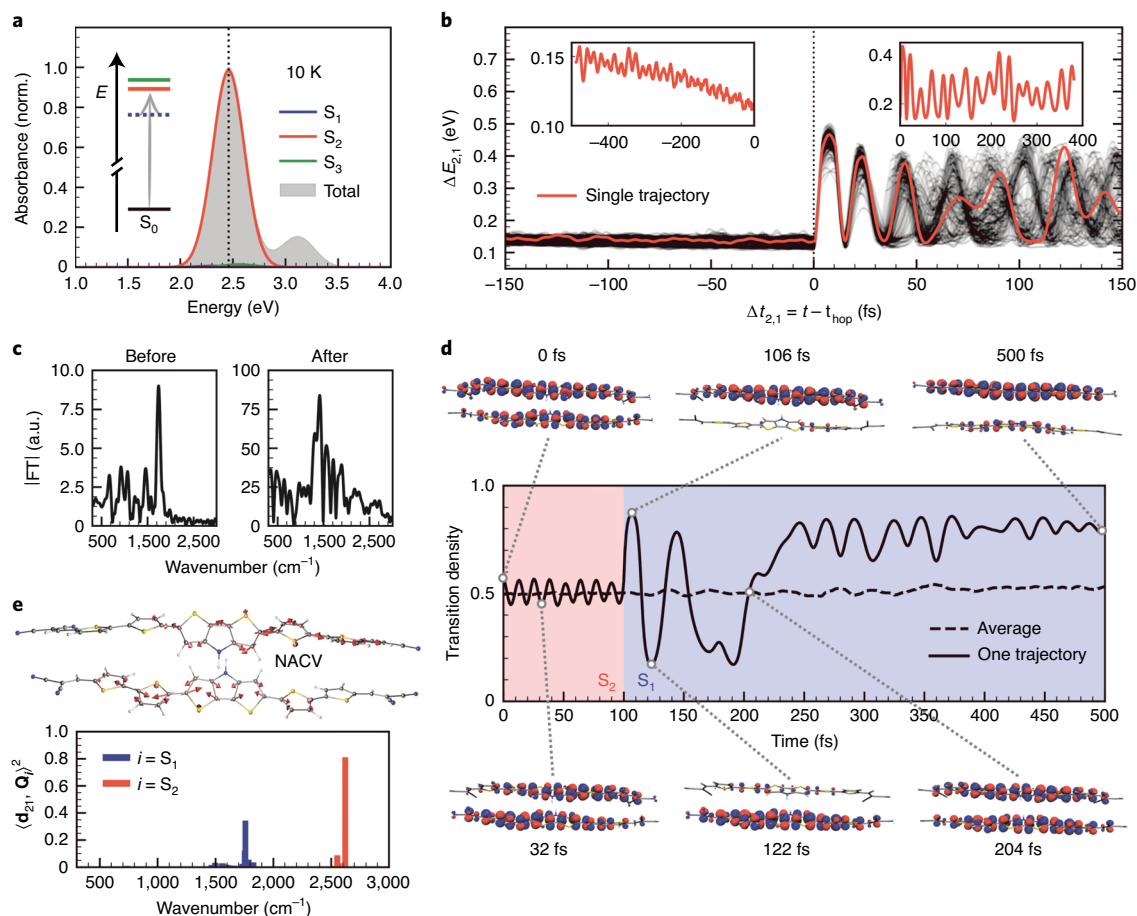
Fig. 3 | Non-adiabatic excited-state molecular dynamics simulations of an A–D–A oligomer dimer. a, Absorption spectrum and (inset) lowest-lying electronic states. The solid (dashed) lines indicate bright (dark) states. **b**, Dynamics of the electronic energy gap $\Delta E_{2,1}$ between S_1 and S_2 states for all trajectories (black) and an exemplary one (red, insets). A jump in $\Delta E_{2,1}$ ($t - t_{hop} = 0$) is the signature of a non-adiabatic transition from S_2 to S_1. **c**, Fourier transform of $\Delta E_{2,1}$ for the exemplary trajectory showing the vibrational mode spectrum (left) before and (right) after the surface crossing. a.u., arbitrary units. **d**, Transition density dynamics on one oligomer unit for (solid) an exemplary trajectory and (dashed) the ensemble average. Snapshots of the orbital plots at selected times show the initial spatial delocalization of the transition density in the S_2 state (red) and its transient localization on one of the oligomers after surface crossing (blue). Transition density oscillations between the two oligomer units persist until the system gets trapped on one of them within roughly 500 fs. **e**, Non-adiabatic coupling vector (NACV, $\mathbf{d}_{2,1}$) between S_1 and S_2 comprising an antisymmetric vibration of the dimer and its projections onto the excited-state instantaneous normal modes for (blue) S_1 and (red) S_2, respectively.

The second excited state S_2 is optically bright and gives the largest contribution to the main absorption resonance at roughly 2.5 eV (Fig. 3a, red line). Both S_1 and S_2 states describe delocalized intermolecular excitations of the dimer. They arise from symmetric (S_2) and antisymmetric (S_1) combinations of the first excited state (S_1^M) intramolecular wavefunctions of the two oligomer units placed in a H-aggregate-like geometry. A weaker resonance at roughly 3 eV derives from higher-lying bright states that are not optically excited in our experiment.

In the dimer simulations, we approximate the dynamics of an optically excited wave packet as an ensemble average over semiclassical trajectories of the nuclear motion that are launched in the Franck–Condon region[43]. Along these trajectories, the relative energy difference between the S_2 and S_1 states, $\Delta E_{2,1}$, initially decays monotonically until, suddenly, it rapidly increases (Fig. 3b). The steep increase in $\Delta E_{2,1}$ indicates a sudden change in slope of the PES experienced by the wave packet. It is thus a direct signature of the unidirectional, non-adiabatic population transfer from S_2 to S_1 and strong evidence for an intermolecular CoIn connecting them. In our simulations, the nuclear configuration at which this hopping

takes place depends on the specific trajectory and may lie in a finite region around the CoIn. After the crossing, large-amplitude oscillations of $\Delta E_{2,1}$ initiate (Fig. 3b). Their frequency spectrum (Fig. 3c, right panel) shows a main peak at roughly 1,500 cm^{-1} together with a distribution of other components. This broad spectrum is consistent with the washout of the 2DES pattern in our experiments. In contrast, the frequency spectrum of the weak oscillations before the crossing (Fig. 3b inset) displays fewer components with the dominant peak now being at roughly 1,700 cm^{-1} (Fig. 3c left panel). Hence, the periods of the optically excited tuning modes are markedly different before and after the crossing.

We further examine the time evolution of the electronic transition density matrix, reflecting the spatial distribution of the optically excited wavefunction[44,45]. Orbital plots of the diagonal elements of the transition density matrix, representing the optically induced changes on each atom, show that the optical excitation is initially delocalized over both oligomer units (Fig. 3d). As long as the system is in the S_2 state, rapid periodic oscillations (roughly 12 fs period) of very small transition density fractions between the oligomer units are seen (Fig. 3d, shaded red). The excitation remains,

however, delocalized over the entire dimer. On transition to S_1, both the amplitude and period of these transition density oscillations dramatically increase, indicating an abrupt change of the PES (Fig. 3d, blue shaded) and a dissipation of an excess of electronic energy into vibrational motion. Moreover, we find that this transition initiates a dynamic localization process of the electronic density on one of the oligomers, followed by pronounced oscillations of the transition density between the two units. This transient localization eventually transforms the coherent intermolecular excitation across the dimer into an intramolecular excitation localized on a single oligomer unit in roughly 500 fs.

To probe the characteristic vibrations driving the electronic $S_2–S_1$ transition, we calculate the non-adiabatic coupling vector (NACV, $d_{2,1}$, Fig. 3e). It indicates the instantaneous direction of the main driving forces along the PES and hence the direction of the population transfer during an electronic transition[42]. Its projection onto the normal modes at the time of the crossing thus reveals an asymmetric high-frequency (roughly 2,600 cm^{-1}) vibration of the dimer as the dominant mode (Fig. 3e and Supplementary Fig. 10, red). We deduce that this asymmetric vibration is directly involved in driving the non-adiabatic transition from S_2 to S_1. Vibronic coupling to such an asymmetric mode is an essential ingredient of CoIns. Thus, we identify this asymmetric vibration as the dominant coupling mode Q_2.

In these low temperature simulations, it takes roughly 400 fs for the population to transfer from S_2 to S_1 (Supplementary Fig. 9b). At room temperature, this transfer time reduces to only around 40 fs (Supplementary Fig. 9a), in excellent agreement with our experiments. This points to the role of thermally induced vibrational fluctuations in bringing the wave packet to the CoIn seam.

Conclusions

Taken together, our experimental and theoretical results provide strong evidence that the passage of a coherent vibrational wave packet through an intermolecular conical intersection governs the ultrafast, sub-100-fs energy transfer dynamics in functional molecular aggregates. The initial impulsive optical excitation populates the lowest optically bright state, spatially delocalized across the aggregate. Coupling to both low- (Q_1) and high-frequency (Q_3) modes drives this coherent intermolecular excitation towards the CoIn. Transition from the bright to the dark state through an asymmetric high-frequency coupling mode (Q_2) triggers dissipation of electronic into vibrational energy and localization within the aggregate. The timescale for initiating this trapping process is governed by the time it takes for the optically launched wave packet to reach and pass the CoIn. Hence, it strongly depends on the details of the vibronic couplings determining the potential energy landscape in the aggregate. As such, intermolecular CoIns control the transition from a coherently moving vibronic wave packet, spatially delocalized across several oligomer units, towards a localized, trapped exciton, whose transport proceeds by classical diffusive hopping. Controlling these initial coherent dynamics thus provides new opportunities for steering the flow of energy and charges and their pathways on the nanoscale in functional assemblies. This requires strategies for precisely shaping vibronic couplings in molecular aggregates and solid-state nanostructures in general. These strategies may range from synthetic chemistry methods, for example to selectively exchange molecular groups in parts of the system[46], to altering the PES by coupling molecular excitations to confined electric fields in for example, cavity structures[47–49], or by controlled structural variations of the molecular arrangement. To this end, donor–acceptor-type oligomer aggregates may represent a versatile platform on which to explore intermolecular CoIns in guiding the ultrafast energy redistribution in technologically relevant systems. Precise control of intermolecular CoIns in such aggregates may enable new routes for the manipulation of nanoscale coherent energy transport in functional nanostructures and may lead to new approaches to the design of optoelectronic devices.

Online content

Any methods, additional references, Nature Research reporting summaries, source data, extended data, supplementary information, acknowledgements, peer review information; details of author contributions and competing interests; and statements of data and code availability are available at https://doi.org/10.1038/s41565-020-00791-2.

References

1. Köppel, H., Domcke, W. & Cederbaum, L. S. in *Advances in Chemical Physics* Vol. 57 (eds Prigogine, I. & Rice, S. A.) 59–246 (John Wiley & Sons, Inc., 2007).
2. Worth, G. A. & Cederbaum, L. S. Beyond Born–Oppenheimer: molecular dynamics through a conical intersection. *Ann. Rev. Phys. Chem.* **55**, 127–158 (2004).
3. Domcke, W. & Yarkony, D. R. Role of conical intersections in molecular spectroscopy and photoinduced chemical dynamics. *Ann. Rev. Phys. Chem.* **63**, 325–352 (2012).
4. Franck, J. & Dymond, E. G. Elementary processes of photochemical reactions. *Trans. Faraday Soc.* **21**, 536–542 (1926).
5. Hader, K., Albert, J., Gross, E. K. U. & Engel, V. Electron-nuclear wave-packet dynamics through a conical intersection. *J. Chem. Phys.* **146**, 5 (2017).
6. Polli, D. et al. Conical intersection dynamics of the primary photoisomerization event in vision. *Nature* **467**, 440–443 (2010).
7. Robb, M. A. in *Advances in Physical Organic Chemistry* Vol. 48 (eds Williams, I. H. & Williams, N. H.) 189–228 (Academic Press, 2014).
8. Kowalewski, M., Fingerhut, B. P., Dorfman, K. E., Bennett, K. & Mukamel, S. Simulating coherent multidimensional spectroscopy of nonadiabatic molecular processes: from the infrared to the X-ray regime. *Chem. Rev.* **117**, 12165–12226 (2017).
9. Wang, Q., Schoenlein, R. W., Peteanu, L. A., Mathies, R. A. & Shank, C. V. Vibrationally coherent photochemistry in the femtosecond primary event of vision. *Science* **266**, 422 (1994).
10. Schapiro, I. et al. The ultrafast photoisomerizations of rhodopsin and bathorhodopsin are modulated by bond length alternation and HOOP driven electronic effects. *J. Am. Chem. Soc.* **133**, 3354–3364 (2011).
11. Johnson, P. J. M. et al. Local vibrational coherences drive the primary photochemistry of vision. *Nat. Chem.* **7**, 980–986 (2015).
12. Schnedermann, C. et al. Evidence for a vibrational phase-dependent isotope effect on the photochemistry of vision. *Nat. Chem.* **10**, 449–455 (2018).
13. Waldeck, D. H. Photoisomerization dynamics of stilbenes. *Chem. Rev.* **91**, 415–436 (1991).
14. Nenov, A. et al. UV-light-induced vibrational coherences: the key to understand Kasha rule violation in trans-azobenzene. *J. Phys. Chem. Lett.* **9**, 1534–1541 (2018).
15. Gueye, M. et al. Engineering the vibrational coherence of vision into a synthetic molecular device. *Nat. Commun.* **9**, 313 (2018).
16. Bhattacherjee, A. et al. Photoinduced heterocyclic ring opening of furfural: distinct open-chain product identification by ultrafast X-ray transient absorption spectroscopy. *J. Am. Chem. Soc.* **140**, 12538–12544 (2018).
17. Yang, J. et al. Imaging CFl3 conical intersection and photodissociation dynamics with ultrafast electron diffraction. *Science* **361**, 64 (2018).
18. Liebel, M., Schnedermann, C. & Kukura, P. Vibrationally coherent crossing and coupling of electronic states during internal conversion in beta-carotene. *Phys. Rev. Lett.* **112**, 198302 (2014).
19. Sobolewski, A. L. & Domcke, W. Ab initio studies on the photophysics of the guanine–cytosine base pair. *Phys. Chem. Chem. Phys.* **6**, 2763–2771 (2004).
20. Groenhof, G. et al. Ultrafast deactivation of an excited cytosine-guanine base pair in DNA. *J. Am. Chem. Soc.* **129**, 6812–6819 (2007).
21. Musser, A. J. et al. Evidence for conical intersection dynamics mediating ultrafast singlet exciton fission. *Nat. Phys.* **11**, 352–357 (2015).
22. Ai, Y. J. et al. Excited-state decay pathways of flavin molecules in five redox forms: the role of conical intersections. *J. Phys. Chem. A* **122**, 7954–7961 (2018).
23. Hore, P. J. & Mouritsen, H. The radical-pair mechanism of magnetoreception. *Ann. Rev. Biophys.* **45**, 299–344 (2016).
24. Hestand, N. J. & Spano, F. C. Expanded theory of H- and J-molecular aggregates: the effects of vibronic coupling and intermolecular charge transfer. *Chem. Rev.* **118**, 7069–7163 (2018).

25. Popp, W., Polkehn, M., Binder, R. & Burghardt, I. Coherent charge transfer exciton formation in regioregular P3HT: a quantum dynamical study. *J. Phys. Chem. Lett.* **10**, 3326–3332 (2019).

26. Settels, V. et al. Identification of ultrafast relaxation processes as a major reason for inefficient exciton diffusion in perylene-based organic semiconductors. *J. Am. Chem. Soc.* **136**, 9327–9337 (2014).

27. Lee, M. H. & Troisi, A. Vibronic enhancement of excitation energy transport: Interplay between local and non-local exciton-phonon interactions. *J. Chem. Phys.* **146**, 075101 (2017).

28. Duan, H.-G., Nalbach, P., Miller, R. J. D. & Thorwart, M. Ultrafast energy transfer in excitonically coupled molecules induced by a nonlocal Peierls phonon. *J. Phys. Chem. Lett.* **10**, 1206–1211 (2019).

29. Popovic, D. et al. Preparation of efficient oligomer-based bulk-heterojunction solar cells from eco-friendly solvents. *J. Mater. Chem. C.* **5**, 9920 (2017).

30. Coughlin, J. E., Henson, Z. B., Welch, G. C. & Bazan, G. C. Design and synthesis of molecular donors for solution-processed high-efficiency organic solar cells. *Acc. Chem. Res.* **47**, 257–270 (2014).

31. Liess, A. et al. Ultranarrow bandwidth organic photodiodes by exchange narrowing in merocyanine H- and J-aggregate excitonic systems. *Adv. Funct. Mater.* **29**, 1805058 (2019).

32. Smits, E. C. P. et al. Near-Infrared light-emitting ambipolar organic field-effect transistors. *Adv. Mater.* **19**, 734–738 (2007).

33. Ben Dkhil, S. et al. Time evolution studies of dithieno[3,2-b:2′,3′-d] pyrrole-based A–D–A oligothiophene bulk heterojunctions during solvent vapor annealing towards optimization of photocurrent generation. *J. Mater. Chem. A.* **5**, 1005–1013 (2017).

34. Jonas, D. M. Two-dimensional femtosecond spectroscopy. *Ann. Rev. Phys. Chem.* **54**, 425–463 (2003).

35. De Sio, A. et al. Tracking the coherent generation of polaron pairs in conjugated polymers. *Nat. Commun.* **7**, 13742 (2016).

36. De Sio, A. & Lienau, C. Vibronic coupling in organic semiconductors for photovoltaics. *Phys. Chem. Chem. Phys.* **19**, 18813–18830 (2017).

37. Pullerits, T., Zigmantas, D. & Sundström, V. Beatings in electronic 2D spectroscopy suggest another role of vibrations in photosynthetic light harvesting. *Proc. Natl Acad. Sci. USA* **110**, 1148 (2013).

38. Romero, E., Novoderezhkin, V. I. & van Grondelle, R. Quantum design of photosynthesis for bio-inspired solar-energy conversion. *Nature* **543**, 355–365 (2017).

39. Jonas, D. M. Vibrational and nonadiabatic coherence in 2D electronic spectroscopy, the Jahn–Teller effect, and energy transfer. *Ann. Rev. Phys. Chem.* **69**, 327–352 (2016).

40. Egorova, D., Gelin, M. F. & Domcke, W. Analysis of cross peaks in two-dimensional electronic photon-echo spectroscopy for simple models with vibrations and dissipation. *J. Chem. Phys.* **126**, 074314 (2007).

41. Nelson, T., Fernandez-Alberti, S., Roitberg, A. E. & Tretiak, S. Nonadiabatic excited-state molecular dynamics: modeling photophysics in organic conjugated materials. *Acc. Chem. Res.* **47**, 1155–1164 (2014).

42. Nelson, T., Fernandez-Alberti, S., Roitberg, A. E. & Tretiak, S. Electronic delocalization, vibrational dynamics, and energy transfer in organic chromophores. *J. Phys. Chem. Lett.* **8**, 3020–3031 (2017).

43. Barbatti, M. Nonadiabatic dynamics with trajectory surface hopping method. *Wiley Interdisc. Rev. Comput. Mol. Sci.* **1**, 620–633 (2011).

44. Tretiak, S. & Mukamel, S. Density matrix analysis and simulation of electronic excitations in conjugated and aggregated molecules. *Chem. Rev.* **102**, 3171–3212 (2002).

45. Wu, C., Malinin, S. V., Tretiak, S. & Chernyak, V. Y. Exciton scattering and localization in branched dendrimeric structures. *Nat. Phys.* **2**, 631–635 (2006).

46. Schuurman, M. S. & Stolow, A. Dynamics at conical intersections. *Ann. Rev. Phys. Chem.* **69**, 427–450 (2018).

47. Herrera, F. & Spano, F. C. Cavity-controlled chemistry in molecular ensembles. *Phys. Rev. Lett.* **116**, 238301 (2016).

48. Galego, J., Garcia-Vidal, F. J. & Feist, J. Suppressing photochemical reactions with quantized light fields. *Nat. Commun.* **7**, 13841 (2016).

49. Gu, B. & Mukamel, S. Manipulating nonadiabatic conical intersection dynamics by optical cavities. *Chem. Sci.* **11**, 1290–1298 (2020).

Methods

Sample preparation. The A–D–A oligomer, comprising dithieno(3,2-*b*:2′,3′-*d*) pyrrole-thiophene as the central donor and two dicyanovinyl units as terminal acceptors, is synthesized and processed according to ref. [29]. To prepare the thin films, the oligomer is dissolved in *O*-xylene in a concentration of 30 mg ml^{-1} and is stirred at 80 °C for >1 h. The thin-film fabrication is conducted by doctor-blading from the hot solutions on 170-µm-thin glass substrates followed by a 30 s solvent–vapour–annealing post-deposition treatment with tetrahydrofuran[29]. This results in thin-film layers with thickness of roughly 100 nm in which the A–D–A oligomer forms small ordered aggregates with typical grain sizes of 20–50 nm (refs. [29,33]). The linear absorption spectrum of the thin-film samples is recorded at room temperature with a Shimadzu SolidSpec-3700 spectrophotometer and is shown in Fig. 1c.

Experimental pump-probe and 2D electronic spectroscopy setup. The differential transmission spectra $\Delta T/T$ and 2DES maps are recorded using a home-built femtosecond spectrometer in a partially collinear pump-probe configuration (Supplementary Fig. 1a). A home-built non-collinear optical parametric amplifier, pumped by the second harmonic of a regeneratively amplified Ti:Sapphire laser (Spectra Physics Spitfire Pro), delivering 150-fs pulses centred at 800 nm with a repetition rate of 5 kHz, is used to generate ultrabroadband pulses with a spectrum ranging from roughly 1.7 to 2.4 eV (Supplementary Fig. 1b), matching the low-energy absorption band of the aggregate thin film (Fig. 1c). Chirped mirrors (Laser Quantum DCM9, not shown in Supplementary Fig. 1) are used to compress the optical pulses. Second harmonic generation frequency-resolved optical gating (Supplementary Fig. 1c) is used to characterize the optical pulses, resulting in a pulse duration of about 8 fs. A broadband beam splitter is used to separate the beam into pump and probe arms. For 2DES, the collinear pump–pulse pair is generated by a common path delay line (TWINS)[50] on the basis of birefringent wedges. To compensate the dispersion introduced by the wedges, an additional pair of chirped mirrors (Laser Quantum DCM10) is put in the pump arm of the setup before the TWINS. The time delay between the two phase-locked pump pulses (coherence time) τ is scanned with a motorized translation stage (Physik Instrumente M122.2DD). To calibrate τ, during the experiment a small fraction of the pump beam is sent to a photodiode that records the time-domain interference signal of the two pump pulses during the measurement[35]. For the two-pulse differential transmission measurements, τ is set to zero.

The waiting time T, defined as the time delay between the pump–pulse pair and the probe beam, is controlled by another motorized translation stage (Physik Instrumente M-111.1DG). Pump and probe beams are focused onto the sample to a spot size of roughly 70 µm with a spherical mirror. The relative polarization between the linearly polarized pump and probe pulses is set to roughly 55°. After the sample, the transmitted probe beam is dispersed in a monochromator and recorded with a 1,024-pixel CCD-array (Entwicklungsbüro Stresing), whereas the transmitted pump beam is blocked. A mechanical chopper in the pump arm modulates the presence of the pump pulses at a frequency of 500 Hz, such that experimentally normalized differential transmission spectra $\frac{\Delta T(\tau,T,E_D)}{T(\tau,T,E_D)} = \frac{T_{on}(\tau,T,E_D)-T_{off}(\tau,T,E_D)}{T_{off}(\tau,T,E_D)}$ are recorded as a function of the time delays τ and T, and of the detection energy E_D. Here T_{on} (T_{off}) denotes the transmitted probe beam intensity spectrum after the sample recorded when the pump is switched on (off). Absorptive 2DES maps $A_{2D}(E_X,T,E_D)$ are obtained by taking the real part of the Fourier transform of the measured signal $\frac{\Delta T(\tau,T,E_D)}{T(\tau,T,E_D)}$ along the coherence time τ, $A_{2D}(E_X, T, E_D) = \text{Re}\left\{ \int_0^\infty \frac{\Delta T(\tau,T,E_D)}{T(\tau,T,E_D)} e^{-i\frac{E_X}{\hbar}\tau} d\tau \right\}$, to obtain the excitation energy E_X axis. Before this, for each T and E_D, all the measured signals are multiplied with a Gaussian filter $G(\tau) = e^{-4\ln 2\left(\frac{\tau}{\tau_F}\right)^2}$, with $\tau_F = 180$ fs the full-width at half maximum, to minimize the effect of truncation on the Fourier transform[35].

Non-adiabatic excited-state dynamics calculations. Simulations of non-adiabatic excited-state dynamics are performed on an antifacial oligomer dimer (Fig. 1c and Supplementary Fig. 8). The side chains are removed to reduce the computational costs. We have used density functional theory (DFT) to generate initial structures of a monomer (oligomer) and the respective dimer. Both systems are optimized using the quantum chemical program package Orca v.4.0.1 (ref. [51]). The CAM-B3LYP (Coulomb attenuating method with Becke, three-parameter, Lee–Yang–Parr) functional[52] in combination with a single-zeta quality all-electron basis set is used and dispersion interactions are taken into account via Grimme's empirical correction according to v.D3 (ref. [53]) with Becke–Johnson damping[54]. The last dispersive corrections are particularly important to simulate realistic interacting dimer configurations. We further use a time-dependent DFT approach with the same functional/basis set to calculate the reference absorption spectra of molecules. These spectra are compared to experiment and serve as benchmark for excited-state structure for a simpler configuration interaction singles (CIS) level combined with the Austin model 1 (AM1) Hamiltonian used for excited-state

dynamics simulations (the method is described below). Overall time-dependent DFT and AM1/CIS approaches produce similar absorption spectra for monomer and dimer (Fig. 3a and Supplementary Figs. 7e and 8a) consistent with experiment (Fig. 1c and Supplementary Fig. 7d) as judged by a pronounced band-gap absorption peak and the overall line shape. Notably, in all the cases theoretical spectra are blue-shifted compared to experiment. For example, absorption spectrum of a dimer is shifted to the blue by about 0.5 eV in AM1/CIS compared to experiment. This is attributed to several reasons. First, our simulations use a dimer, being a minimal model, instead of larger aggregates present in the experiments. Moreover, dielectric medium effects absent in the simulations, cause red shifts in the spectra. Second, the semiempirical level of theory is not exact and typically has an accuracy 0.2–0.4 eV when describing absorption spectra of conjugated molecules, as exemplified in a recent review[55]. These comparisons allow us to identify the essential excited states participating in the dynamics and to prepare an initial photoexcitation consistent with spectroscopic probes for our dynamical simulations.

The semiempirical non-adiabatic excited-state molecular dynamics (NEXMD) package (https://github.com/lanl/NEXMD)[55] is further used for all dynamical simulations of excited states. The NEXMD relies on an improved Tully's fewest switches surface hopping algorithm[56] for modelling non-adiabatic dynamics as described in detail in the recent review[55], which exemplifies many previous successful NEXMD applications. In the fewest switches surface hopping algorithm, the probability of the hop is chosen in a Monte Carlo-like fashion with hopping probability being proportional to the square of the non-adiabatic coupling vector.

$$\mathbf{d}_{\alpha\beta} = \left\langle \phi_\alpha(\mathbf{r}; \mathbf{R}(t)) | \nabla_\mathbf{R} \phi_\beta(\mathbf{r}; \mathbf{R}(t)) \right\rangle, \tag{1}$$

where $\mathbf{r}$ and $\mathbf{R}(t)$ are the electronic and nuclear vector coordinates, respectively, $\nabla_\mathbf{R}$ stands for differentiation with respect to nuclear coordinates, and $\phi_\alpha(\mathbf{r}; \mathbf{R}(t))$ $\left(\phi_\beta(\mathbf{r}; \mathbf{R}(t))\right)$ is the CIS adiabatic wavefunction of the αth (βth) electronic state. The direction of $\mathbf{d}_{\alpha\beta}$ corresponds to the direction of the main force on the nuclei during strong non-adiabatic interactions between αth and βth electronic states[55]. All ingredients for non-adiabatic dynamics such as excited-state energies, gradients, transition density matrices and non-adiabatic coupling vectors are calculated 'on the fly' at AM1/CIS level as implemented in NEXMD[57]. A 1-ns constrained ground state trajectories at room (300 K) and low (10 K) temperature are performed to collect 500 snapshots of initial configurations for the excited-state dynamics. The Langevin thermostat and a friction coefficient $\gamma = 20.0$ ps is used. During the constrained ground state simulations, six atomic coordinates are held fixed (Supplementary Fig. 8) to compensate for the lack of dispersion corrections in the semiempirical approach. The optical spectrum is generated from 500 single-point calculations by averaging over all spectra from all geometries. The total optical absorbance A for all excitation energies Ω is broadened by a Gaussian line shape and weighted by the oscillator strength f of each excited state $|\alpha\rangle$ included,

$$A(\Omega) = \frac{1}{N_i} \sum_i^{N_i} \sum_\alpha^{N_\alpha} f_\alpha^i(\Omega_\alpha) \times \frac{1}{\sqrt{2\pi\sigma^2}} \exp\left[-\frac{(\Omega_\alpha - \Omega)^2}{2\sigma^2} \right]. \tag{2}$$

The index i runs over all geometries N_i, whereas the index α over all excited-state energies N_α. A simulated laser pulse is used to populate the initial excited state for each configuration according to the Franck–Condon window, given by

$$g_\alpha(\mathbf{r}, \mathbf{R}) = \left(\frac{f_\alpha}{\Omega_\alpha^2} \right) \exp\left[-\sigma^2 (E_{laser} - \Omega_\alpha)^2 \right]. \tag{3}$$

Here, E_{laser} represents the central energy of the laser pulse and is taken as 2.44 eV (2.46 eV) for the calculations at 300 K (10 K). The excitation energy width is given by the transform-limited relation of a Gaussian laser pulse $f(t) = \exp(t^2/2\sigma^2)$ with a full-width at half maximum of 12 fs, giving a standard deviation of $\sigma = 0.15$ eV ($\sigma = 0.25$ eV) for 300 K (10 K). A classical time step of 0.1 fs and a quantum time step of 0.025 fs have been used for the propagation of nuclear and electronic degrees of freedom, respectively. Electronic decoherence is taken into account using an instantaneous decoherence procedure[58] where coefficients are reinitialized after successful and attempted hops. The evolution of the entire ensemble of trajectories defines the dynamics of the photoexcited wave packet and thus relevant to experimental relaxation timescales (Fig. 3b). In addition, characteristic trajectory examples are chosen to analyse representative dynamics of wavefunctions and vibrational degrees of freedom. Here, the spatial extent of the wavefunctions is examined using transition density matrices[44],

$$(\rho^{0\alpha})_{nm} = \left\langle \phi_\alpha(\mathbf{r}; \mathbf{R}(t)) | c_n^\dagger c_m | \phi_0(\mathbf{r}; \mathbf{R}(t)) \right\rangle, \tag{4}$$

where $c_n^\dagger$ (c_m) are creation (annihilation) operators, n and m denote atomic orbital basis functions and $\phi_0(t)$ and $\phi_\alpha(t)$ are the ground and excited-state wavefunctions. Therefore, the diagonal elements $(\rho^{0\alpha})_{nn}$ represent the net change in the electronic density induced on an atomic orbital for a ground to excited-state electronic

transition (Fig. 3d and Supplementary Figs. 7b and 8b). The normalization condition $\sum_{nm} (\rho^{0\alpha})^2_{nm} = 1$ holds for the CIS approximation[59]. In this scheme, the fraction of the transition density localized on either the top or bottom oligomer unit of the dimer can be calculated by adding the contributions from each atom i in the X ($X =$ top, bottom) oligomer unit as follows,

$$(\rho^{0\alpha})^2_X = \sum_{n_i m_i, i \in X} (\rho^{0\alpha})^2_{n_i m_i}. \tag{5}$$

At a given time, the intramolecular vibrations are described as a set of well-defined and independent harmonic oscillators[60]. The gradients are calculated analytically, whereas the second derivatives are obtained numerically. When the Hessian matrix is diagonalized, a set of excited-state instantaneous normal mode $\mathrm{ES-INM}(S_\alpha)$ vectors $\{Q^i_\alpha\}_{i=1,3N}$ can be expressed as a linear combination of Cartesian displacements $\partial \mathbf{R}$,

$$Q^i_\alpha(t) = \sum_{j=1}^{3N} l^{ij}_\alpha \partial \mathbf{R}^j_t, \tag{6}$$

where l^{ij}_α are coefficients of the corresponding eigenvector matrix L_α. Projection of the non-adiabatic coupling vector $\mathbf{d}_{2,1}$ on the basis of $\mathrm{ES-INM}(S_2)$ and $\mathrm{ES-INM}(S_1)$ at the moment of transition t_{hop} is given by

$$\mathbf{d}_{2,1}(t_{\mathrm{hop}}) = \sum_{j}^{3N-6} a^j_2(t_{\mathrm{hop}}) Q^j_2(t_{\mathrm{hop}}) = \sum_{j}^{3N-6} b^j_1(t_{\mathrm{hop}}) Q^j_1(t_{\mathrm{hop}}). \tag{7}$$

where coefficients a^j_2 and b^j_1 reflect participation of vibrational modes of the first and second excited states, respectively.

Data availability
The data that support the findings of this study, large data sets stored in the data repositories of different institutions in different countries, are available from the authors upon reasonable request.

Code availability
The NEXMD code is available at https://github.com/lanl/NEXMD. This program is open source under the BSD-3 Licence.

References

50. Brida, D., Manzoni, C. & Cerullo, G. Phase-locked pulses for two-dimensional spectroscopy by a birefringent delay line. *Opt. Lett.* **37**, 3027–3029 (2012).
51. Neese, F. The ORCA program system. *Wiley Interdiscip. Rev.: Computational Mol. Sci.* **2**, 73–78 (2012).
52. Yanai, T., Tew, D. P. & Handy, N. C. A new hybrid exchange–correlation functional using the Coulomb-attenuating method (CAM-B3LYP). *Chem. Phys. Lett.* **393**, 51–57 (2004).
53. Grimme, S., Antony, J., Ehrlich, S. & Krieg, H. A consistent and accurate ab initio parametrization of density functional dispersion correction (DFT-D) for the 94 elements H-Pu. *J. Chem. Phys.* **132**, 154104 (2010).
54. Grimme, S., Ehrlich, S. & Goerigk, L. Effect of the damping function in dispersion corrected density functional theory. *J. Comput. Chem.* **32**, 1456–1465 (2011).
55. Nelson, T. R. et al. Non-adiabatic excited-state molecular dynamics: theory and applications for modeling photophysics in extended molecular materials. *Chem. Rev.* **120**, 2215–2287 (2020).
56. Tully, J. C. Molecular dynamics with electronic transitions. *J. Chem. Phys.* **93**, 1061–1071 (1990).
57. Nelson, T., Naumov, A., Fernandez-Alberti, S. & Tretiak, S. Nonadiabatic excited-state molecular dynamics: on-the-fly limiting of essential excited states. *Chem. Phys.* **481**, 84–90 (2016).
58. Nelson, T., Fernandez-Alberti, S., Roitberg, A. E. & Tretiak, S. Nonadiabatic excited-state molecular dynamics: treatment of electronic decoherence. *J. Chem. Phys.* **138**, 224111 (2013).
59. Tretiak, S., Isborn, C. M., Niklasson, A. M. N. & Challacombe, M. Representation independent algorithms for molecular response calculations in time-dependent self-consistent field theories. *J. Chem. Phys.* **130**, 054111 (2009).
60. Soler, M. A., Roitberg, A. E., Nelson, T., Tretiak, S. & Fernandez-Alberti, S. Analysis of state-specific vibrations coupled to the unidirectional energy transfer in conjugated dendrimers. *J. Phys. Chem. A* **116**, 9802–9810 (2012).

Author contributions
A.D.S., P.B. and C.L. initiated this project. D.P., E.M.-O. and P.B. synthesized the materials and prepared the thin films. E.S., X.T.N. and A.D.S. performed the experiments. E.S., A.D.S. and C.L. analysed the data. S.P, C.A.R., E.M., L.G., B.T.N., T.F. and S.T. performed quantum chemical modelling of the molecular structure and optical spectra. L.G., B.T.N., S.F.-A., T.F. and S.T. performed non-adiabatic dynamics simulations. A.D.S. and C.L. wrote the manuscript with important contributions from all authors.

Competing interests
The authors declare no competing interests.

Additional information
Supplementary information is available for this paper at https://doi.org/10.1038/s41565-020-00791-2.

Correspondence and requests for materials should be addressed to A.D.

Peer review information *Nature Nanotechnology* thanks Oleg Prezhdo and the other, anonymous, reviewer(s) for their contribution to the peer review of this work.

Reprints and permissions information is available at www.nature.com/reprints.